Threshold Shock Sensor Based on a Bistable Mechanism: Design, Modeling, and Measurements

Attilio Frangi, Biagio De Masi, Federica Confalonieri, and Sarah Zerbini

I. Introduction

SEVERAL standards like the MIL-STD-202G Method 213B [2] or the Jedec JESD22-B104C [3] prescribe tests having the purpose of determining the suitability of component parts and sub-assemblies of electrical and electronic components when subjected to shocks such as those resulting from rough handling, transportation and real-life operations. During these tests the components are subjected to acceleration histories with given shape (e.g. half-sine, saw-tooth), maximum g value (from 30g to 1500g in [2]) and test duration (from 0.5 ms to 11 ms in [2]).

Passive sensors are an emerging class of devices, still not controlled by an industrial standard, designed to detect and record mechanical shocks due to mishandling of fragile or calibrated products inducing accelerations exceeding those prescribed by the standard against which the products have been certified.

Manuscript received March 5, 2015; revised July 22, 2015; accepted July 24, 2015. Date of publication August 19, 2015; date of current version November 25, 2015. This work was supported by STMicroelectronics, Cornaredo, Italy. Subject Editor D. Elata.

A. Frangi, B. De Masi, and F. Confalonieri are with the Dipartimento di Ingegneria Civile e Ambientale, Politecnico di Milano, Milan 20133, Italy (e-mail: attilio.frangi@polimi.it; biagiodemasi@gmail.com; federica.confalonieri@polimi.it).

S. Zerbini is with the AMS Division, STMicroelectronics, Cornaredo 20010, Italy (e-mail: sarah.zerbini@st.com).

Color versions of one or more of the figures in this paper are available online.

Passive shock sensors are inexpensive and the power consumption is negligible, but in general their control of the threshold is somewhat approximate. For instance, [4] describes a semiconductor shock sensor, which comprises a supporting body and a movable mass connected together by suspension springs having weakening regions. If the acceleration exceeds a given threshold, the weakening regions break. However, these sensors suffer from a large spread in the material rupture strength.

Several contributions in the literature have tried to provide an estimate of the rupture strength σ_R of polysilicon: e.g. the experiments performed in [5] suggest $\sigma_R = (1.88 \pm 0.33)$ GPa; in [6] one finds $\sigma_R = (2.24 \pm 0.35)$ GPa; [7] proposes $\sigma_R = (1.21 \pm 0.16)$ GPa. It is hence quite evident that not only σ_R strongly depends on the fabrication process, but even for a fixed process it presents large uncertainties. This scatter adds to the classical variability due to overetch which dramatically affects stress concentrations.

Other types of shock sensors, as described in [8], are based upon a chamber containing a conductive liquid and having a wall configured to break due to an impact. The same document describes also shock sensors that comprise a magnetic element held suspended by a conductive spring between metal walls. In either case, the structures are rather complicated and hardly compatible with standard ICs processes.

The aim of the present contribution is to discuss and analyse a shock sensor originally proposed in [1] and [9] that reduces the limitations described above and, in particular, may be conveniently used in portable electronic devices. The sensor has been fabricated with the ThELMA (Thick Epitaxial Layer for Microactuators and Accelerometers) process (see e.g. [10]) which is based on the growth, over a sacrificial silicon oxide layer, of a thick epitaxial silicon layer that is finally released.

The present device avoids the scatter due to rupture strength because it is based on the transition between two stable configurations of elastic beams (described in the following sections) which depends on geometrical parameters and mechanical properties that are easier to control during the fabrication. A schematic drawing of the device is presented in Figure 1. A suspended inertial mass (shuttle) is attached to the substrate via the central anchor point and four flexible springs. The mass is surrounded by four bistable elements (composite beams) that are initially in their first stable configuration. When an external acceleration reaches a given threshold (say 1000g for the device analysed, where g is the acceleration of gravity), the contact force transmitted by the mass to the bistable element induces the transition to a second

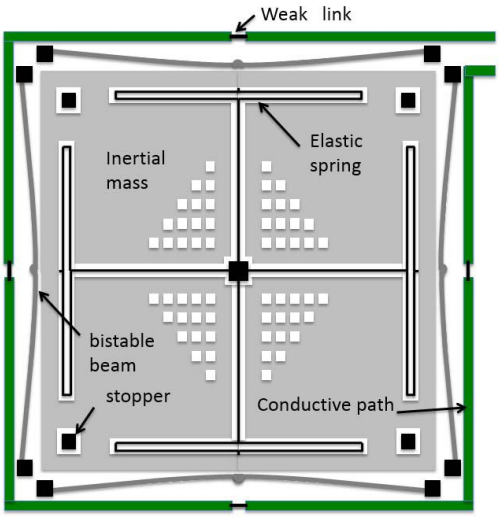

Fig. 1. Sketch of the device. The bistable beams are in the first equilibrium configuration.

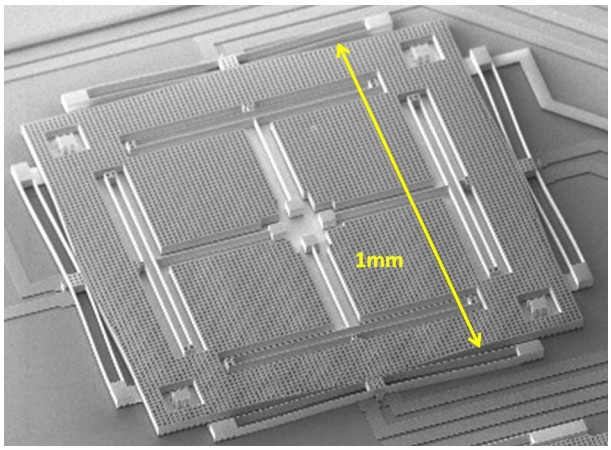

Fig. 2. SEM of whole fabricated device.

stable configuration. During the dynamical transition the beam hits a weak link that breaks and opens a resistive path. The energy released during the snap-through is much larger than the rupture energy of the link ([11]).

When required, the new status can be detected by measuring this variation of resistance. The SEM of the fabricated device in its rest configuration is shown in Figure 2.

A key part of the sensor is represented by the bistable elements. Multistable elements are often utilized for various applications ([12]) including energy harvesting ([13], [14]) even at the microscale [15]. Multistability can be achieved in several ways, e.g. exploiting the magnetic field produced by permanent magnets or piezoelectric effects ([16], [17]). Limiting our attention to the mechanical multistability of beams, the simplest possible multistable beam is a doubly clamped straight beam compressed above the Eulerian critical load. There are two stable equilibrium configurations that are perfectly symmetric with respect to the original beam axis. However, the production and control of such a device poses formidable challenges if it has to be fabricated with standard industrial surface micro-machining processes. An alternative practical way for producing a bistable element is to design a doubly clamped beam with a deformed initial shape.

Following an idea put forward by [18] and [19], each bistable element is made of two doubly clamped beams fabricated with the initial stress-free deflection $w_0(x) = \delta/2(1-\cos(2\pi x/L))$, δ being the initial displacement of the beam at midspan, L its length, and x a coordinate running along the beam axis from one anchor point to the other. It is worth stressing that a single doubly clamped beam with the given initial configuration w_0 is not bistable: the central clamp between the two beams eliminates the possibility of antisymmetric deformation modes and restores bistability, as will be better explained in Section II.

The paper is organized as follows. In Section II the design parameters of the sensor are given and the mathematical model is established by applying the theory of slender beams subjected to moderately large displacements. In Section III the model is solved numerically with two different approaches providing an estimate of the acceleration threshold inducing the snap-through. The predictions are verified experimentally in Section IV where the results of tests on 163 devices are summarized. Finally some conclusions are drawn in Section VI. Both the experimental tests and the numerical simulations are conducted with acceleration histories based on the standards [2], [3]. In particular, the reference test has a sinusoidal external acceleration with frequency equal to 1500 Hz.

II. Design and Modelling

The sensor is made of polysilicon having mechanical properties that have been thoroughly investigated in [10]. Herein we assume linear elastic isotropic constitutive behavior with Young modulus $E = 150$ GPa and mass density $\rho = 2330$ kg/m^3. The out of plane thickness of the device is fixed by the fabrication process to $H = 22$ μm. The gap with the substrate is 1.8 μm.

The central suspended shuttle, of mass $M = 1.95\times10^{-8}$ kg, is attached to the substrate via four flexible springs; each of these springs is made of 5 thin elements of thickness $t_s = 2.6$ μm and length $L_s = 245$ μm.

The shuttle in its rest condition is positioned very close (with a gap of approximately 1 μm) to four bistable elements, each made of two doubly clamped beams that have the initially curved shape analytically described by:

$$w_0 = \delta\phi_1(x) \quad \text{with} \quad \phi_1 = \frac{1}{2}\left(1-\cos\frac{2\pi x}{L}\right) \tag{1}$$

with $\delta = 10$ μm, $L = 600$ μm.

The two doubly-clamped beams are rigidly connected to each other in the central portion by a clamp in order to prevent rotation. As well known in the literature ([18], [19]), a single doubly-clamped beam with initial configuration given by eq.(1) is not bistable. Indeed, if forced to the second equilibrium configuration (bottom of Figure 3) it would snap back to the first configuration (top of Figure 3) via an anti-symmetric mode that is prevented here by means of the central clamp. Therefore, only symmetric deflections of the bistable elements will be considered in the following. Moreover a bistable mechanism can be obtained only if the curved beams are characterized by a sufficiently high

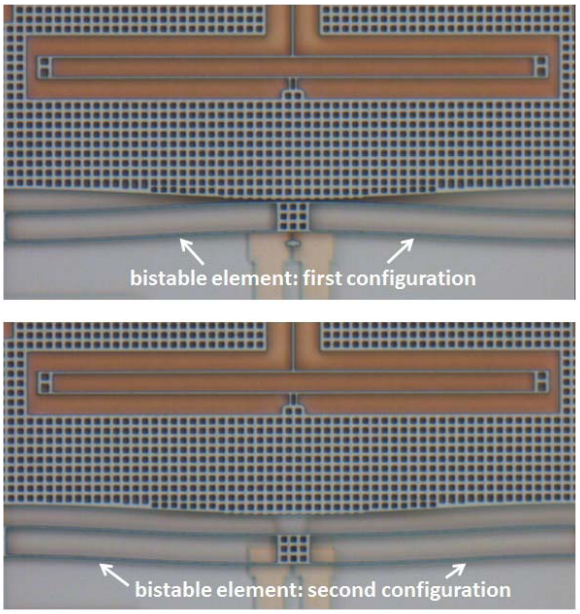

Fig. 3. Zoom on the bistable element in the two stable configurations before and after actuation.

geometrical coefficient $\Delta = \delta/t$, where t is the in-plane (vibrating) thickness. The ratio Δ has to respect the inequality $\Delta > 4/\sqrt{3}$ which sets an upper bound on t. In the current design of the device $t = 2$ μm and hence $\Delta = 5$.

If the bistable element is loaded quasi-statically with a force F applied at mid-span, its displacement is initially proportional to the first buckling mode, i.e. $w = \alpha\phi_1(x)$. Setting $y = \alpha/\delta$ and $\Delta = \delta/t$ the force-displacement relationship is:

$$F(y) = 2\frac{\pi^4 EI}{L^3}(\delta-\alpha)\left(2+\frac{3}{2t^2}\alpha(\delta+\alpha)\right) = 2\frac{\pi^4 EI\delta}{L^3}(1-y)\left(2+\frac{3}{2}\Delta^2 y(1+y)\right) \quad (2)$$

The force which induces the snap-through is a parameter of paramount importance. As discussed in [19], since $\Delta^2 > 16/3$, snap-through occurs when the stiffness of the third buckling mode vanishes, i.e. when:

$$y_{\mathrm{T}}^2 = 1 - \frac{16}{3\Delta^2} \quad (3)$$

and the snap-through force F_{T} follows from eq.(2) as $F_{\mathrm{T}} = F(y_{\mathrm{T}})$. Formulas (2)-(3) have been used for the preliminary design of the sensor, but are approximate since a quasi-static behaviour is assumed.

In order to reproduce the experiments reported in Section IV, we discuss here a more sophisticated dynamical model including contact. With the aim of simplifying as much as possible the underlying equations, we assume that the substrate is subjected to the external in-plane acceleration a aligned with the device as depicted in Figure 4, and that the movement occurs along the same direction.

Contact will develop only with one bistable element.

The stiffness of the spring system of the shuttle (see Figure 1) has been computed with standard procedures

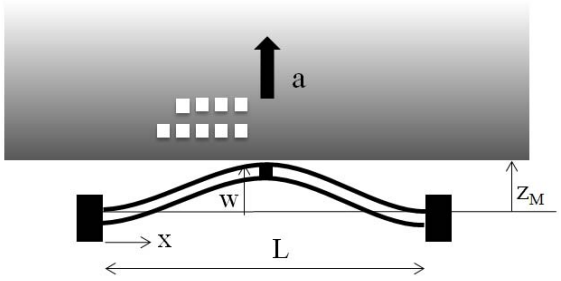

Fig. 4. Simplified scheme: rigid shuttle and bistable element. The coordinates system is attached to the anchors. z_M denotes the shuttle position.

as $K \simeq 11$ N/m. The Couette flow between the mass and the substrate generates a dissipative force $C\dot{z}_M$. Using the techniques of [20] and [21] a quality factor $Q = 40$ has been estimated. If contact is activated between the mass and the bistable element, the mass will receive the force P. Globally, in a frame rigidly connected with the anchors, the shuttle dynamics is governed by the 1D model

$$M(\ddot{z}_M + a) + C\dot{z}_M + K(z_M - \delta) = P \quad (4)$$

where z_M denotes the mass coordinate.

The beam dynamics can be described via the Principle of Virtual Power for slender beams and moderately large displacements (see e.g. [23]–[26]), with the addition of the inertia forces. For each of the two beams in the bistable element the problem is formulated as follows. Find the deflection $w(x) \in \mathcal{C}'(0)$ such that, for $\forall\tilde{w} \in \mathcal{C}'(0)$:

$$\int_0^L \Big(\rho A(\ddot{w}+a)\tilde{w} EI(w''-w_0'')\tilde{w}'' - N[w]w'\tilde{w}'\Big)\mathrm{d}x = -\frac{P}{2}\tilde{w}(L/2) \quad (5)$$

The space $\mathcal{C}'(0)$ is here the space of functions w with continuous first derivative and $w = w' = 0$ in $x = 0, L$. and

$$N[w] = \frac{EA}{2L}\int_0^L \Big((w_0')^2 - (w')^2\Big)\,\mathrm{d}x = -EA\frac{\Delta L}{L}$$

is the compressive axial force assumed independent of the position along the beam (ΔL is the elongation of the beam axis). The force $-P$ is exerted by the shuttle on the central clamp when contact develops and is assumed to be equally distributed between the two beams. $A = Ht$ is the cross section area of each beam; $I = (1/12)Ht^3$ is the modulus of inertia; ρA is the mass per unit length; EI is the flexural stiffness. It is worth to underline that the term $EI(w''-w_0'')$ represents the bending moment in the beam and that the rotational inertia of the cross sections has been neglected.

The two equations (4) and (5) must be complemented with the conditions

$$z_M - w(L/2) \geq 0, \quad P > 0 \quad (z_M - w(L/2))P = 0 \quad (6)$$

governing "perfectly hard" contact. The first of (6) prevents penetration between the beam and the shuttle; the second guarantees that the force exchanged is repulsive and the third

simply states that the force arises only when the gap is closed and vanishes otherwise.

III. Numerical Results

A. Simplified Approach

In order to solve eq.(5) numerically, the simplest possible solution strategy consists in assuming a two-dimensional discretization space such that the displacement w is expressed as a linear combination of the first and third buckling modes:

$$w(x,t) = \alpha(t)\phi_1(x) + \beta(t)\phi_3(x)$$

where ϕ_1 is defined in eq.(1) and:

$$\phi_3 = \frac{1}{2}\left(1 - \cos\frac{4\pi x}{L}\right) \tag{7}$$

Initial conditions impose $w = w_0$ and hence $\alpha(0) = \delta$ and $\beta(0) = 0$. It is worth recalling that ϕ_1 and ϕ_3 are the buckling modes of a doubly clamped straight beam. The second antisymmetric mode:

$$\phi_2 = 1 - \frac{2x}{L} - \cos\left(N_1\frac{x}{L}\right) + \frac{2}{N_1}\sin\left(N_1\frac{x}{L}\right) \tag{8}$$

(with $N_1 \simeq 2.86\pi$) is constrained by the presence of the central clamp.

Setting first $\tilde{w} = \phi_1$ and then $\tilde{w} = \phi_3$ in eq.(5), one gets two second-order differential equations for α and β:

$$\rho AL\left(\frac{3\ddot{\alpha}}{8} + \frac{a}{2} + \frac{\ddot{\beta}}{4}\right) + EI\frac{2\pi^4}{L^3}(\alpha - \delta) - \frac{\pi^2}{2L}N[\alpha,\beta]\alpha = -\frac{P}{2}$$

$$\rho AL\left(\frac{\ddot{\alpha}}{4} + \frac{a}{2} + \frac{3\ddot{\beta}}{8}\right) + EI\frac{32\pi^4}{L^3}\beta - \frac{2\pi^2}{L}N[\alpha,\beta]\beta = 0$$

with:

$$N[\alpha,\beta] = EA\frac{\pi^2}{2L^2}\left(\frac{\delta^2}{2} - \frac{\alpha^2}{2} - 2\beta^2\right) \tag{9}$$

A penalty approach is implemented to simulate contact. This consists in replacing perfectly hard contact with a contact force linearly increasing with compenetration:

$$P = \lambda(\alpha - z_M)H(\alpha - z_M)$$

where H is the Heaviside function and λ is a positive large penalty coefficient. This set of equations is integrated with an explicit central difference scheme and adaptive step control.

Figures 5-7 present the simulated history of the mid-span deflection $\alpha = w(L/2)$ computed by applying an external acceleration of the form:

$$a(t) = \frac{Ng}{2}(1 - \cos(2\pi f_0 t)) \quad t < \frac{1}{f_0}, \tag{10}$$

Three different values of the acceleration frequency have been considered, with $f_0 = 500$ Hz, $f_0 = 1500$ Hz and $f_0 = 5000$ Hz, respectively. The choice $f_0 = 1500$ Hz corresponds to the experiments described in Section IV. The simulations have been run for increasing values of maximum acceleration Ng in order to identify the threshold acceleration a_T inducing the transition to the second stable configuration. At each frequency, the response for two values of N_g just below and above a_T is presented. In the former case the beam goes back to the initial configuration; in contrast, in the latter situation contact is lost at a certain time and the beam makes the transition to the second stable equilibrium configuration.

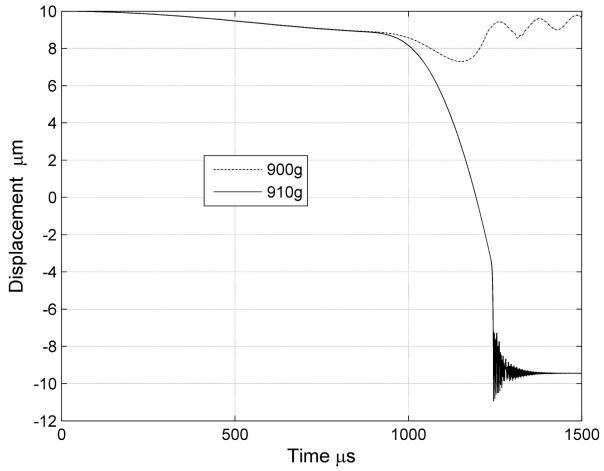

Fig. 5. Simulated midspan deflection for two different values of Ng (see eq. 10) just below and above the snap-through threshold. Input frequency 500 Hz.

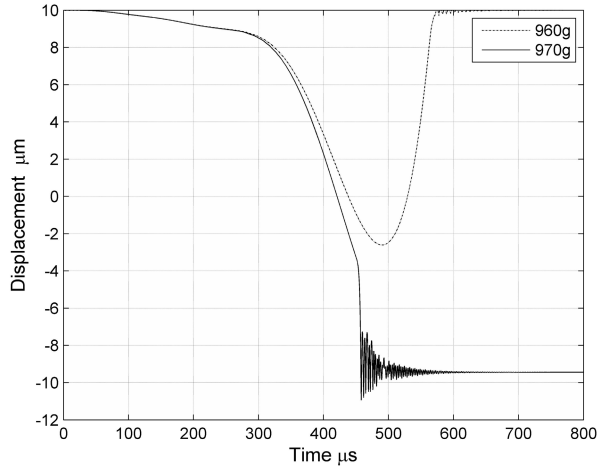

Fig. 6. Simulated midspan deflection for two different values of Ng (see eq. 10) just below and above the snap-through threshold. Design input frequency 1500 Hz.

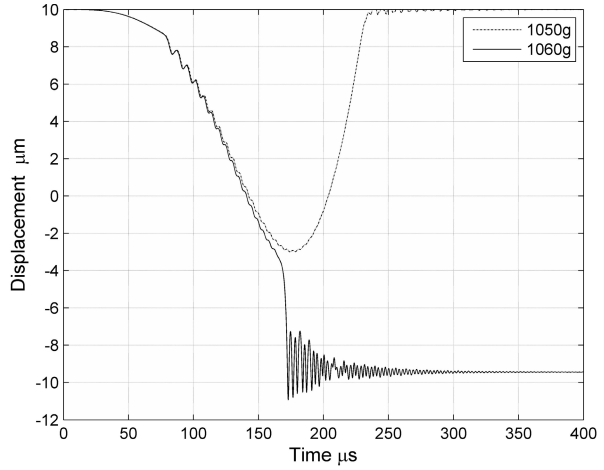

Fig. 7. Simulated midspan deflection for two different values of Ng (see eq. 10) just below and above the snap-through threshold. Input frequency 5000 Hz.

Even if the range of the investigated frequencies is extremely large, only a 10% scatter of the critical acceleration is found.

B. Comparison With the Complete Model

In order to verify the accuracy of the simplified model discussed in the previous section, eq.(5) is now solved using a standard Finite Element procedure. The beam is divided into N elements with cubic Hermite shape functions. When the generalized displacement field $w(x,t) = \Phi(x)\mathbf{W}(t)$ and the test function $\tilde{w}(x,t) = \Phi(x)\tilde{\mathbf{W}}(t)$ (where Φ is the shape function matrix) is inserted into eq.(5), a system of semi-discretized equations is obtained:

$$\begin{aligned}\mathbf{M}\ddot{\mathbf{W}}(t) + \left(\mathbf{K}_e + N\left[\mathbf{W}(t)\right]\mathbf{K}_g\right)\mathbf{W}(t) \\ = \mathbf{F}_{ext}(t) + \mathbf{F}_0 - \mathbf{F}_{in}(t) \quad \forall\tilde{\mathbf{W}}\end{aligned} \tag{11}$$

with:

$$\mathbf{M} = \int_0^L \rho A \Phi^T \Phi \mathrm{d}x$$

$$\mathbf{F}_{in} = \int_0^L \rho A \Phi^T a(t) \mathrm{d}x$$

$$\mathbf{F}_0 = \int_0^L E J \Phi''^T \delta\phi_1'' \mathrm{d}x$$

$$\mathbf{K}_e = \int_0^L E J \Phi''^T \Phi'' \mathrm{d}x$$

$$\mathbf{K}_g = \int_0^L \Phi'^T \Phi' \mathrm{d}x$$

In the above equations $\mathbf{M}$ is the mass matrix; $\mathbf{K}_e$ is the elastic stiffness matrix; $\mathbf{K}_g$ is the geometric stiffness matrix; $\mathbf{F}_{ext}$, $\mathbf{F}_0$, and $\mathbf{F}_{in}$ are vectors of equivalent nodal forces, taking into account the contact force exerted by the rigid shuttle, the effect of the initial deflection and that of the external acceleration. As in section III, the contact between the rigid shuttle, whose dynamics is described by eq.(4), and the bistable beam is imposed via a penalty method. An explicit central difference integration scheme is adopted for both systems.

Figure 8 shows the simulated history of the mid-span deflection $w(L/2)$ for an input acceleration frequency equal to $f_0 = 1500$ Hz, corresponding to the experimental value. Results are compared with the 970g acceleration history of Figure 6. Also in this case the predicted threshold acceleration inducing snap-through is between 960g and 970g. With respect to the results of the 2DOF model, in a first loading phase the beam is less stiff due to the richer space of admissible displacements; however, when the critical load is approached, the displacements of the structure are actually accurately described by the two buckling modes and the simplified model correctly reproduces the snap-through transition.

IV. Experimental Results

The fabricated device, having a nominal shock threshold of 1000g, has been initially tested with an external mechanical point acting on the central mass and imposing a sufficiently large displacement so as to induce the transition of the bistable

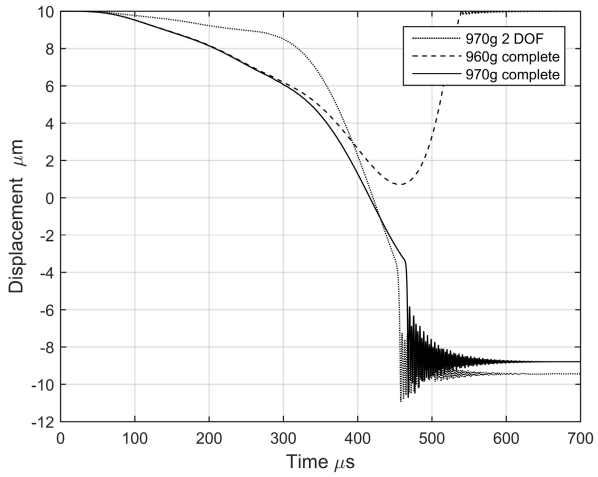

Fig. 8. Beam discretized with 10 Hermite elements. Simulated midspan deflection for two different values of external acceleration just below and above the snap-through threshold. The results obtained with the 2DOF model are plotted for comparison. Design input frequency 1500 Hz.

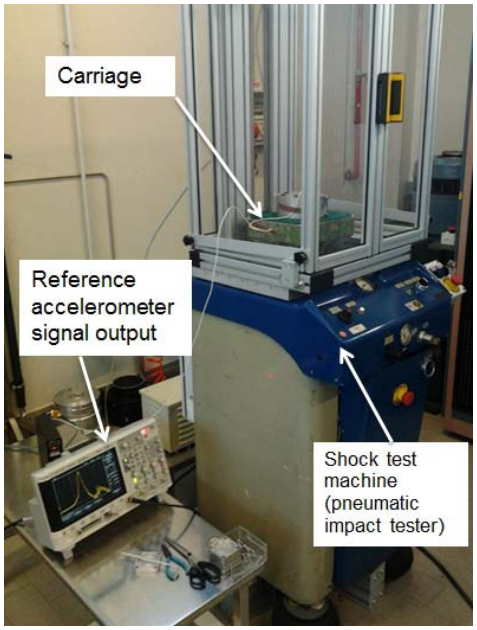

Fig. 9. Experimental apparatus.

elements to the second stable state as illustrated in Figure 3 in the top picture.

Next a series of quantitative shock tests have been performed on an AVCO shock tester AVEX SM105 (shown in Figure 9) that is capable of providing half-sine shock pulses with different durations and amplitudes.

Chips have been attached to a frame undergoing the controlled acceleration histories. Typical shock shapes are collected in Figure 10. The accelerations, measured by accurate reference accelerometers co-mounted with the devices, are plotted with respect to time. The shock pulse duration is chosen according to the MIL.STD-202G protocol [2] which is typically adopted to check the suitability of electronic components when subjected to

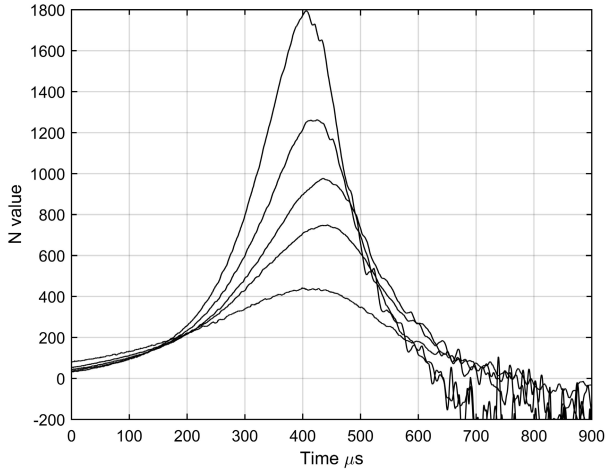

Fig. 10. Typical acceleration histories imposed on the chips.

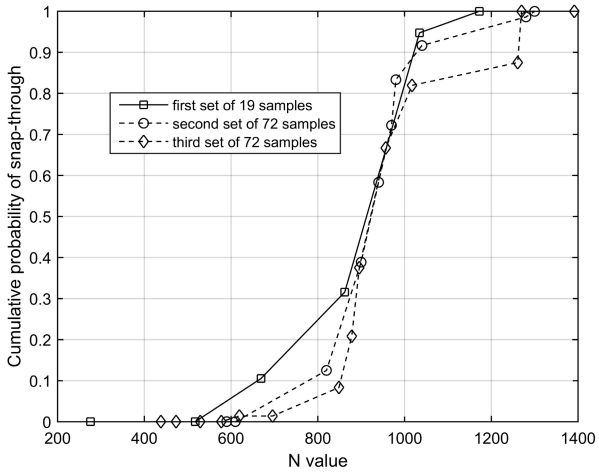

Fig. 11. Cumulative probability of rupture vs. maximum acceleration.

improper handling, transportation and in general operations that have as consequence a mechanical shock.

Each history is characterized by the parameter N such that Ng denotes the maximum value of the acceleration of the test itself (e.g. 750g, or 970g etc).

Chips have been attached to the frame with two orientations (a) or (b), rotated of 90° with respect to (a), such that the maximum acceleration occurs along a direction orthogonal to a couple of opposite bistable mechanisms.

The tests have been conducted as follows. All the chips have been subjected to a series of shock tests with increasing maximum acceleration and the number of ruptures has been recorded. The results are summarized in Figure 11 where the cumulative probability of rupture (the sum of the two orientations) is plotted always versus the maximum N value of the test.

In order to better interpret the experimental data, we fit them with the Weibull distribution, the cumulative failure probability function taking the following form:

$$y = 1 - e^{-(x/c)^m}, \quad x = \frac{N}{1000}$$

The shape parameter m, and the characteristic lifetime parameter c are determined using a nonlinear fitting procedure

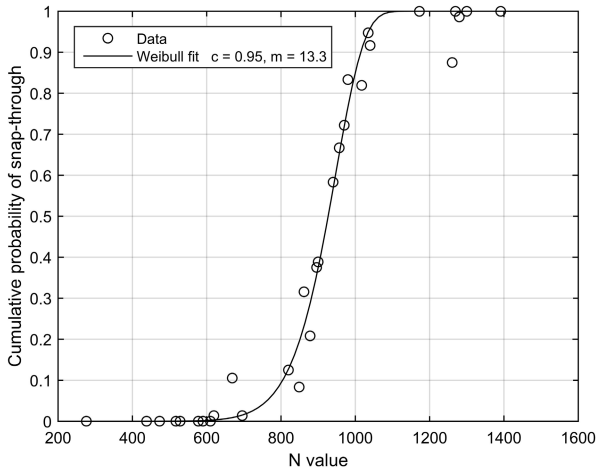

Fig. 12. Weibull fit of the experimental data.

of the experimental data, obtaining:

$$c = 0.9528, \quad m = 13.2978$$

The mean value and the root mean square deviation of the threshold acceleration a_T are computed using the fitted values of the Weibull model yielding Figure 12:

$$a_T = (916 \pm 84)g$$

The experimental results obtained are promising and show a relatively limited scatter, especially if compared to threshold shock sensors based on rupture strength alone. These issues are discussed further in the next section.

V. Discussion and Optimization

A. Scatter Due to Overetch

The sensor proposed helps avoid the variability of rupture strength in classical shock sensors, but it shares the same process uncertainties of most of the existing inertial sensors, like accelerometers and gyroscopes. Uncertainties are mainly due to technological difficulties in controlling over-etching of the suspended features and in particular of the thin beams of the bistable element.

Even if the analytical formulas (2)-(3) are approximate, they give clear indications about the sensitivity of the snap-through force F_{T} (and hence of the threshold acceleration a_{T}) with respect to the overetch. Due to overetch, the stiffness of the beams decreases, although this effect is partially compensated by the decrease of the mass with holes and by the decrease of y_{T}. Finally one obtains that the sensitivity of a_{T} with respect to overetch is -1.2 g/nm. Assuming 0.1 μm as upper bound for the double-sided overetch (i.e. the actual variation of the beam thickness) in a well calibrated etching phase, one gets a maximum variation $\Delta a_{\mathrm{T}} = \pm 120g$. Applying the simulation tool including dynamics and contact (as detailed in section III) this estimate reduces to $\Delta a_{\mathrm{T}} = \pm 90g$. The numerical dispersion is similar to the experimental dispersion discussed in Section IV.

However, this scatter can be reduced through proper redesign of the device. A simple modification consists in

increasing the thickness t_B of the bistable elements in order to reduce the impact of the over-etch uncertainties; at the same time, in order to maintain the overall stiffness, its length L_B should be increased. Setting 1200 μm as an upper bound for the device dimensions, and fixing the desired acceleration threshold to 1000g, an optimization routine has been implemented in order to identify the optimal value of the thickness t_B and length L_B of the bistable element and of the global stiffness K of the springs connecting the shuttle to the anchors.

A device with $t_B = 4.3$ μm, $L_B = 1200$ μm and $K = 3$ N/m has been identified as almost optimal. Numerical simulations show that it guarantees a reduced variation $\Delta a_{\mathrm{T}} = \pm 30g$ for a double-sided overetch of 0.1 μm.

B. Eigenfrequencies of the Bistable Elements

An additional possible issue for the shock sensor is that the transition between the two states of the bistable elements might be triggered by an external acceleration of limited amplitude at frequencies close to the eigenfrequencies of the elements. The small vibrations around equilibrium configurations can be analysed expressing the displacement field as

$$w(x,t) = \alpha\phi_1(x) + u(x,t) \tag{12}$$

where $\alpha\phi_1(x)$ is the equilibrium deflection and $|u| \ll |\alpha\phi_1|$ denotes a small perturbation. The equation governing the free vibrations is obtained by linearising eq.(5) around $\alpha\phi_1$ and can be expressed as follows. Find $u \in \mathcal{C}'(0)$

$$\int_0^L \left(\rho A\ddot{u}\tilde{w} + EIu''\tilde{w}''\right) \mathrm{d}x + \frac{EA}{4L^2}\pi^2(\alpha^2-\delta^2)\int_0^L u'\tilde{w}'\mathrm{d}x + \frac{EA}{L}\alpha^2\int_0^L u'\phi_1'\mathrm{d}x\int_0^L \phi_1'\tilde{w}'\mathrm{d}x = 0 \tag{13}$$

$\forall\tilde{w} \in \mathcal{C}'(0)$. This model, implemented in Matlab, shows that the first eigen-mode in the original configuration ($\alpha = \delta$) has a frequency of $f_1 = 150$ kHz. Moreover, f_1 decreases only slightly for small values of the contact force. Since the power spectrum of external accelerations of interest is negligible at f_1, the device design is robust.

VI. Conclusions

We have discussed a novel passive MEMS shock sensor based on the bistability properties of elastic beams. The sensor has been tested experimentally and simulated numerically. The very good agreement between experiments and numerical simulations on the real devices is encouraging and gives indications for the fabrication of a family of improved shock sensors.

Indeed, experiments show a scatter in the threshold acceleration which is mainly due to uncertainties in the amount of over-etch. This is particularly critical for thin elements like springs. Using the simulation tools validated with the existing device, a redesign has been proposed leading to a reduced sensitivity to overetch.

The proposed device only senses in-plane accelerations, and is not isotropic, in the sense that it has two preferential directions, i.e. those associated with the orientation of the bistable mechanisms. Two simple provisions could solve this shortcoming. More shock sensors could be used in parallel, with relative orientations optimized in order to improve isotropy (e.g. 45° in the case of two devices). Alternatively, the square mass could be replaced by e.g. an hexagonal mass having bistable mechanisms along each edge.

In the design and simulations residual stresses have not been accounted for due to their very low values typical of the ThELMA process; if larger, they could well influence the stability threshold and the dynamics of the transition between the two states.

Acknowledgment

The authors would like to thank Fabio Banfi (ST microelectronics) for the assistance in the testing and measurements.

References

[1] A. Frangi, B. De Masi, F. Confalonieri, and L. Baldasarre, "Threshold shock sensor based on a bi-stable mechanism," in *Proc. TRANSDUCERS* Barcelona, Spain, Jun. 2013, pp. 626–629.

[2] *Test method standard electronic and electrical*, Component Parts, MILSTD-202G, 2002.

[3] *Mechanical Shock*, document JESD22-B104-B, 2014.

[4] *Threshold Acceleration Sensor*, Nokia Corp. ST Microelectron., EP1394555 B1, 2004.

[5] F. Cacchione, M. de Masi, A. Corigliano, and M. Ferrera, "Rupture tests on polysilicon films through on-chip electrostatic actuation [MEMS applications]," in *Proc. 5th Int. Conf. EuroSimE*, 2004, pp. 347–350.

[6] D. A. LaVan and T. E. Buchheit, "Strength of polysilicon for MEMS devices," *Proc. SPIE*, pp. 40–44, Aug. 1999.

[7] W. N. Sharpe, Jr., Y. Yuan, and R. L. Edwards, "A new technique for measuring the mechanical properties of thin films," *J. Microelectromech. Syst.*, vol. 6, no. 3, pp. 193–199, Sep. 1997.

[8] S. P. Zadesky and F. R. Rothkopf, "Mounted shock sensor," U.S. Patent 2011 0100124 A1, May 5, 2011.

[9] A. Frangi, B. D. Masi, and L. Baldasarre, "Shock sensor with bistable mechanism and method of shock detection," U.S. Patent 2014 0033964 A1, Feb. 6, 2014.

[10] A. Corigliano, B. de Masi, A. Frangi, C. Comi, A. Villa, and M. Marchi, "Mechanical characterization of polysilicon through on-chip tensile tests," *J. Microelectromech. Syst.*, vol. 13, no. 2, pp. 200–219, Apr. 2004.

[11] A. Corigliano, F. Cacchione, A. Frangi, and S. Zerbini, "Numerical modelling of impact rupture in polysilicon microsystems," *Comput. Mech.*, vol. 42, no. 2, pp. 251–259, Jul. 2008.

[12] L. L. Howell, *Compliant Mechanisms*. Hoboken, NJ, USA: Wiley, 2001.

[13] S.-M. Jung and K.-S. Yun, "Energy-harvesting device with mechanical frequency-up conversion mechanism for increased power efficiency and wideband operation," *Appl. Phys. Lett.*, vol. 96, no. 11, p. 111906, 2010.

[14] B. Andó, S. Baglio, G. L'Episcopo, and C. Trigona, "Investigation on mechanically bistable MEMS devices for energy harvesting from vibrations," *J. Microelectromech. Syst.*, vol. 21, no. 4, pp. 779–790, Aug. 2012.

[15] M. R. Brake, M. S. Baker, N. W. Moore, D. A. Crowson, J. A. Mitchell, and J. E. Houston, "Modeling and measurement of a bistable beam in a microelectromechanical system," *J. Microelectromech. Syst.*, vol. 19, no. 6, pp. 1503–1514, Dec. 2010.

[16] M. Ferrari, V. Ferrari, M. Guizzetti, D. Marioli, and A. Taroni, "Piezoelectric multifrequency energy converter for power harvesting in autonomous microsystems," *Sens. Actuators A, Phys.*, vol. 142, no. 1, pp. 329–335, Mar. 2008.

[17] F. Cottone, L. Gammaitoni, H. Vocca, M. Ferrari, and V. Ferrari, "Piezoelectric buckled beams for random vibration energy harvesting," *Smart Mater. Struct.*, vol. 21, no. 3, p. 035021, 2012.

[18] J. Qiu, J. H. Lang, and A. H. Slocum, "A centrally-clamped parallel-beam bistable MEMS mechanism," in *Proc. IEEE MEMS*, Jan. 2001, pp. 353–356.

[19] J. Qiu, J. H. Lang, and A. H. Slocum, "A curved-beam bistable mechanism," *J. Microelectromech. Syst.*, vol. 13, no. 2, pp. 137–146, Apr. 2004.

[20] A. Frangi, "A fast multipole implementation of the qualocation mixed-velocity–traction approach for exterior Stokes flows," *Eng. Anal. Boundary Elements*, vol. 29, no. 11, pp. 1039–1046, Nov. 2005.
[21] A. Frangi, G. Spinola, and B. Vigna, "On the evaluation of damping in MEMS in the slip–flow regime," *Int. J. Numer. Methods Eng.*, vol. 68, no. 10, pp. 1031–1051, Dec. 2006.
[22] R. Ardito, C. Comi, A. Corigliano, and A. Frangi, "Solid damping in micro electro mechanical systems," *Meccanica*, vol. 43, no. 4, pp. 419–428, Aug. 2008.
[23] A. H. Nayfeh, W. Kreider, and T. J. Anderson, "Investigation of natural frequencies and mode shapes of buckled beams," *AIAA J.*, vol. 33, no. 6, pp. 1121–1126, 1995.
[24] C. Comi, "On geometrical effects in micro-resonators," *Latin Amer. J. Solids Struct.*, vol. 6, no. 1, pp. 73–87, 2009.
[25] C. Maurini, J. Pouget, and S. Vidoli, "Bistable buckled beam: Modelling and piezoelectric actuation," *Adv. Sci. Technol.*, vol. 54, pp. 281–286, Sep. 2009.
[26] G. Giannopoulos, J. Monreal, and J. Vantomme, "Snap-through buckling behavior of piezoelectric bimorph beams: I. Analytical and numerical modeling," *Smart Mater. Struct.*, vol. 16, no. 4, p. 1148, 2007.